Available online at www.sciencedirect.com

SciVerse ScienceDirect

Geochimica et Cosmochimica Acta 91 (2012) 171–186

Geochimica et Cosmochimica Acta

www.elsevier.com/locate/gca

Heterogeneous oxidation of Fe(II) on iron oxides in aqueous systems: Identification and controls of Fe(III) product formation

Philip Larese-Casanova *, Andreas Kappler [1], Stefan B. Haderlein [1]

Center for Applied Geosciences, Eberhard-Karls-University Tuebingen, Hölderlinstr. 12, 72076 Tuebingen, Germany

Received 5 January 2012; accepted in revised form 30 May 2012

Abstract

The aqueous Fe(II)–oxide Fe(III) system is a reactant for many classes of redox sensitive compounds via an interfacial Fe(II) sorption and electron transfer process. The poorly soluble Fe(III) products formed as a result of contaminant reduction and Fe(II) oxidation on iron oxides may be capable of modifying iron oxide surfaces and affecting subsequent reduction rates of contaminants such as halogenated ethenes or nitroaromatic compounds. The scope of this study was to identify the secondary Fe(III) mineral phases formed after Fe(II) oxidation on common iron oxides during heterogeneous contaminant reduction by directly targeting the secondary minerals using Mössbauer-active isotopes. Fe(III) mineral characterization was performed using ^{57}Fe-Mössbauer spectroscopy, μ-X-ray diffraction, and electron microscopy after oxidation of dissolved ^{57}Fe(II) using nitrobenzenes as a model oxidant in pH-buffered suspensions of ^{56}hematite, ^{56}goethite, ^{56}magnetite, and ^{56}maghemite. Mössbauer spectra confirmed sorbed ^{57}Fe(II) becomes oxidized by the parent ^{56}Fe(III)-oxide sorbent and assimilated as the sorbent oxide prior to any nitrobenzene reduction, consistent with several reports in the literature. In addition to oxide sorbent growth, Fe(II) sorption and oxidation by nitrobenzene result also in the formation of secondary Fe(III) minerals. Goethite formed on three hematite morphologies (rhombohedra, needles, and hexagonal platelets), and acicular needle shapes typical of goethite appeared on the micron-sized hexagonal platelets, at times aligned in 60° orientations on (0 0 1) faces. The proportion of goethite formation on the three hematites was linked to number of surface sites. Only goethite was observed to form on a goethite sorbent. In contrast, lepidocrocite was observed to form on magnetite and maghemite sorbents (consistent with homogeneous Fe(II) oxidation by O_2) and assumed spherulite morphologies. All secondary Fe(III) phases were confirmed within μ-X-ray diffraction patterns. On hematite, the directed formation of goethite as opposed to lepidocrocite suggests hematite may possess a templating ability for the α-FeOOH atom arrangement as opposed to γ-FeOOH. The initiation of all secondary Fe-oxide formations occurred after four to six equivalents of monolayer coverage on the supporting mineral sorbent. Overall, Fe(III) product identity formed during heterogeneous Fe(II) oxidation appears to be governed mainly by the identity of the underlying sorbent and partly by the amount of available surface sites.
© 2012 Elsevier Ltd. All rights reserved.

1. INTRODUCTION

Iron minerals are ubiquitous in subsurface environments, and iron redox chemistry is closely linked to solution geochemistry (e.g. O_2) and to the transformation of groundwater contaminants. Over the past 20 years, numerous reports have shown the combination of dissolved Fe(II) and Fe(III)-bearing minerals to be a potent reductant for

* Corresponding author. Present address: Department of Civil & Environmental Engineering, Northeastern University, 360 Huntington Avenue, Boston, MA 02115, USA. Tel.: +1 617 373 2899; fax: +1 617 373 4419.

E-mail addresses: phil@coe.neu.edu (P. Larese-Casanova), haderlein@uni-tuebingen.de (S.B. Haderlein).

[1] Tel.: +49 7071 2973148; fax: +49 7071 5059.

0016-7037/$ - see front matter © 2012 Elsevier Ltd. All rights reserved.
http://dx.doi.org/10.1016/j.gca.2012.05.031

many organic and inorganic contaminants including nitroaromatics (Klausen et al., 1995; Charlet et al., 1998; Elsner et al., 2004; Williams and Scherer, 2004; Hartenbach et al., 2006), explosives (Gregory et al., 2004; Nefso et al., 2005), chlorinated solvents (Buchholz et al., 2011), pesticides (Strathmann and Stone, 2003; Nano and Strathmann, 2008), metals (Charlet et al., 1998, 2002; Buerge and Hug, 1999; Peretyazhko et al., 2008), and nitrite (Sorensen and Thorling, 1991; Charlet et al., 1998). Fe(III)-bearing oxides and hydroxides (such as goethite (α-FeOOH), hematite (α-Fe_2O_3), and magnetite (Fe_3O_4), hereafter collectively termed "Fe-oxides") provide reactive surface sites that can sorb Fe(II) atoms and aqueous oxidants and couple the transfer of electrons between them. These surface sites are envisioned as terminal oxygen or hydroxide ligand groups, usually of some partial negative charge, bonded to one or more structural iron cations and capable of complex formation with aqueous Fe(II) (and other multivalent metal cations) in inner-sphere configurations. This process of heterogeneous Fe(II) oxidation and contaminant reduction may be partly responsible for contaminant mitigation within anoxic, Fe(II)-rich aquifers (Rügge et al., 1998). Moreover, natural oxidants such as O_2 and nitrite (NO_2^-) (Sorensen and Thorling, 1991; Park and Dempsey, 2005) can promote heterogeneous Fe(II) oxidation and contribute to the formation of Fe-oxides of varying size, crystallinity, purity, and order in redox-active soils and sediments (Thompson et al., 2006, 2011). Fe(II)–Fe(III) redox reactions are also important for microbial respiration (Lovley, 1997), microbial energy derivation (Konhauser et al., 2011), and contaminant transformation within zero-valent iron systems (Scherer et al., 1999).

An accounting of Fe speciation on Fe-oxides could lead to an improved understanding of electron transfer in heterogeneous systems. In particular, understanding coupled oxidant–iron redox reactions is paramount for evaluating the relative importance of iron-mediated reactions compared to other natural attenuation processes; to this end, these prior studies report rates, extents, product distributions, and geochemical influences on redox reactions. Oxidant half-lives can be minutes (e.g., nitrobenzenes (Klausen et al., 1995)) to months (e.g., trichloroethene (Zwank et al., 2005)) and are strongly influenced by Fe(II) concentration (Strathmann and Stone, 2003), solution pH (Klausen et al., 1995; Pecher et al., 2002; Strathmann and Stone, 2003), and mineral phase (Klausen et al., 1995; Buerge and Hug, 1999; Schultz and Grundl, 2000; Strathmann and Stone, 2003; Elsner et al., 2004). Depending on oxidant class, electron transfer to the oxidant molecule may result in reduction of an organic moiety, reduction of the central metal ion, reductive precipitation of a metal, or reductive dechlorination (Borch et al., 2010). Concomitantly, aqueous Fe(II) must be consumed, oxidized to Fe(III), and presumably accumulate at the iron oxide surface (Amonette et al., 2000; Williams and Scherer, 2004).

This study focuses on understanding the fate of Fe(II) after oxidation to poorly soluble Fe(III) coupled to contaminant reduction on iron oxide surfaces. Reactive surface sites on Fe(III)-oxides must be accessible, and sufficient dissolved Fe(II) must be available, in order for iron-mediated heterogeneous contaminant reduction to be a sustained, viable reaction process throughout the life of a contaminant plume. However, Fe(II)–Fe(III) redox reactions may alter Fe-oxide surfaces, perhaps becoming restructured by precipitation reactions (Hansel et al., 2005; Chun et al., 2006; Yanina and Rosso, 2008), forming new iron phases (Pecher et al., 2002), increasing in reactive surface area (Klupinski et al., 2004), all of which may promote or inhibit contaminant reaction rates (Klausen et al., 1995; Chun et al., 2006). Fe(III) mineralogy is sensitive to geochemical solution condition when formed via oxidation of Fe(II) by O_2 (Cornell and Schwertmann, 2003) or by microbes (Larese-Casanova et al., 2010a,b). In the case of heterogeneous contaminant reduction, repeated sorption and oxidation of Fe(II) on Fe(III)-oxide surfaces will certainly result in the accumulation of new Fe(III) atoms. Identifying the type and morphology of newly precipitated Fe(III) will help us determine to what extent iron mineral surfaces assimilate Fe(III) atoms or form new iron phases.

Recent microscopic, spectroscopic, and computational evidence for reactions of aqueous Fe(II) with Fe(III)-oxide surfaces provide an improved picture of Fe(II)–Fe(III) surface redox chemistry. Uptake of Fe(II) on Fe(III)-oxides alone (in the absence of an external oxidant such as a contaminant or O_2), by way of complexing with surface oxygen atoms, may result in electron transfer from sorbed Fe(II) to oxide Fe(III) and the formation of new Fe(III) which becomes assimilated as part of the Fe(III)-oxide sorbent (Williams and Scherer, 2004; Silvester et al., 2005; Larese-Casanova and Scherer, 2007a; Cwiertny et al., 2008; Yanina and Rosso, 2008; Gorski and Scherer, 2009; Catalano et al., 2010). The injected valence electrons may be transferred rapidly among Fe(III) atoms (Kerisit and Rosso, 2006; Larese-Casanova and Scherer, 2007b), reductively dissolve structural Fe(III) (Pedersen et al., 2005), and induce phase transformations by reprecipitation or structural rearrangement (Zhang et al., 1992; Hansel et al., 2005). Prolonged Fe(II)–Fe(III) redox cycling may result in face-specific Fe dissolution and deposition of hematite (Yanina and Rosso, 2008), formation of less crystalline rinds (Hansel et al., 2004; Chun et al., 2006), and promote interfacial Fe atom mixing (Crosby et al., 2005; Handler et al., 2009; Mikutta et al., 2009). The presence of a reducible contaminant promotes further sorption and oxidation of aqueous Fe(II) (Amonette et al., 2000; Williams and Scherer, 2004) and the insoluble Fe(III) formed may alter Fe-oxide surfaces, for example the observed lengthening of goethite rods (Chun et al., 2006) or growth of nanosized iron oxide particles (Klupinski et al., 2004).

Identifying the newly formed Fe(III) phases is difficult because of the challenges in detecting usually small amounts of iron atoms and in distinguishing newly precipitated Fe(III) from the parent Fe-oxide substrate using most spectroscopic techniques. Fe(II) oxidation products on non-iron mineral substrates may not have these barriers to analysis and, in fact, have been identified as hematite (as a result of oxidation by pertechnetate on α-Al_2O_3 (Peretyazhko et al., 2008)) and goethite (as a result of oxidation by nitrobenzene on γ-Al_2O_3 (Larese-Casanova et al., 2010a,b)) using ^{57}Fe-Mössbauer spectroscopy. In this work, we employ a ^{57}Fe-Mössbauer technique (Williams and

Scherer, 2004; Larese-Casanova and Scherer, 2007a; Cwiertny et al., 2008; Gorski and Scherer, 2009; Amstaetter et al., 2010; Rosso et al., 2010) to directly observe only the reacted Fe(II) (as ^{57}Fe) and not the underlying iron oxide (as ^{56}Fe) during heterogeneous Fe(II) oxidation for a variety of geochemical solution conditions. This technique can distinguish oxidation states, identify mineral phases and relative abundances, and provide insight to crystallinity and magnetic ordering for the reacted ^{57}Fe surface atoms. Such information gathered from ^{57}Fe-Mössbauer spectroscopy has been valuable for understanding a variety of redox-driven processes that influence iron mineral identity and morphology, including interfacial electron transfer processes with contaminants (Williams and Scherer, 2004), mineral surface topology changes (Rosso et al., 2010), microbial metabolism (Frankel et al., 1983), and weathering of natural iron minerals (Thompson et al., 2006).

Here, nitrobenzene was used as model oxidant because, unlike O_2, it oxidizes Fe(II) associated with oxides but not aqueous Fe(II), eliminating homogeneous oxidation of aqueous Fe(II), and is common among heterogeneous contaminant studies. The ^{56}Fe-oxides used were goethite, magnetite, maghemite, and three morphologies of hematite, all thermodynamically stable and resistant to drastic phase transformations during reactions with Fe(II). Because contaminant reduction rates, and therefore Fe(II) sorption and oxidation rates, are dependant on solution pH, dissolved Fe(II) concentration, and Fe(III) mineral type, we expect these geochemical parameters to affect the identity and abundance of Fe(II) oxidation products.

2. METHODS

2.1. Reagents

Anoxic stock solutions of Mops (3-(N-morpholino)propanesulfonic acid) Good's buffer, NaCl, and NaOH were prepared using N_2-purged, deoxygenated, deionized water within an anoxic glovebox with a 100% N_2 atmosphere. HCl solutions were made by diluting N_2-purged concentrated HCl with deoxygenated, deionized water. Acidic solutions of ^{57}Fe(II) were made by dissolving ^{57}Fe(0) (99% pure, Chemgas) powder in 2 M HCl solution and filtered prior to use (Williams and Scherer, 2004). Acidic solutions of ^{56}Fe(II) were prepared in a similar manner using ^{56}Fe(0) (99.94% pure, Chemgas). Separate anoxic stock solutions of 4-chloro-nitrobenzene and 4-methyl-nitrobenzene were prepared by dissolving weighed amounts of the nitrobenzene solids into N_2-purged, deoxygenated methanol. All solutions were prepared within an anoxic glovebox.

2.2. ^{56}Fe-oxide synthesis

^{56}Hematite rhombohedra crystals were synthesized according to a modified hydrothermal method (Raming et al., 2002). A 340 mM solution of ^{56}Fe(II) was removed from the glovebox, and the Fe(II) was oxidized to Fe(III) by incremental addition of hydrogen peroxide while stirring. The solution turned brown and was allowed to rest for several hours. The solution was then filtered through a 0.45 μm syringe-tip filter and diluted with deionized water to a 260 ml, 20 mM Fe(III) solution that was capped in a Schott® bottle and heated at 100 °C for 7 days during which a red precipitate formed. The precipitate was collected by centrifugation at 12,000*g*, resuspended and washed in 10 mM NaCl, centrifuged again, and dried for 7 days at 50 °C.

^{56}Goethite was synthesized according to a modified method of ferrihydrite conversion (Schwertmann and Cornell, 2000). A 4 ml, 1.8 M solution of ^{56}Fe(II) was removed from the glovebox, and the Fe(II) was oxidized to Fe(III) by addition of hydrogen peroxide while stirring within a plastic bottle. The solution was then filtered, and the pH was raised to 12.0 by addition of 5 M KOH, forming a brown precipitate. The suspension was diluted with deionized water to 110 mL, capped, and heated at 65 °C for 4 days. The yellow-ochre precipitate was collected by centrifugation at 10,000*g*, resuspended and washed in 10 mM NaCl, centrifuged again, and dried for 3 days at 50 °C.

^{56}Hematite hexagons were synthesized according to a modified method in which ^{56}goethite was converted to ^{56}hematite under hydrothermal conditions (Sugimoto and Wang, 1998). Two hundred and seventy milligrams of ^{56}goethite were added to 5.4 ml of 8.0 M NaOH solution within a pressure-sealed Teflon container and heated to 250 °C for 6 h. After cooling, the red–purple precipitate was centrifuged at 10,000*g*, washed in deionized water, centrifuged again, and dried for 3 days at 100 °C.

^{56}Hematite needles were converted from acicular ^{56}goethite by heating to 450 °C for 24 h (Duvigneaud and Derie, 1980).

^{56}Magnetite was synthesized according to a modified method of Fe(II)–Fe(III) coprecipitation (Cornell and Schwertmann, 2003). A 15 ml, 133 mM ^{56}Fe(II) solution was removed from the glovebox and oxidized to ^{56}Fe(III) using H_2O_2 while stirring. This solution was purged again with N_2 gas and returned to the glovebox. The pH was raised to about 5 by addition of 15 M NaOH, and a brown precipitate formed. The solution became very warm, so it was cooled with ice until room temperature. A 30 ml, 133 mM ^{56}Fe(II) solution was then added to the ^{56}Fe(III) solution, stirred, and titrated to pH 10 using 15 M NaOH. A black precipitate formed and was stirred for 12 h. The precipitates were collected by centrifugation at 10,000*g* and dried within the glovebox for 4 days. The dried precipitates were crushed, sieved, and washed quickly in deoxygenated, deionized water to dissolve NaCl crystals that may have formed during drying. The powder was dried again as previously described. The Fe(II):Fe(III) stoichiometry was measured by dissolving a small amount in 6 M HCl and measuring the dissolved Fe(II) concentration and the total Fe concentration (after reduction with hydroxylamine hydrochloride) with the ferrozine method. A Fe(II):Fe(III) value of 0.27 was observed, which is less than the stoichiometric value of 0.50.

^{56}Maghemite was synthesized according to a modified method of thermal conversion of magnetite (Cornell and Schwertmann, 2003). ^{56}Magnetite was heated to 190 °C for 36 h, and the powder turned from black to brown. To check if complete oxidation of Fe(II) to Fe(III) occurred,

a small amount was dissolved in 6 M HCl, and the Fe(II) content was only 1% of the total dissolved Fe.

The purity of all synthesized ^{56}Fe oxides was confirmed with μ-XRD. All oxides were sieved with a 45-μm sieve prior to use. Oxides were weighed to a mass of 15.0 mg within Eppendorf tubes and stored within the anoxic glovebox to allow O_2 to diffuse away from the oxide surface.

2.3. Fe(II) oxidation and nitrobenzene reduction experiments

All batch reactor experiments were performed within an anoxic glovebox in N_2 atmosphere. The appropriate volume of ^{57}Fe(II) to make a final concentration of about 3 mM was added to a solution of 30 mM Mops and 30 mM NaCl. The pH was adjusted to the desired value using 0.5 M NaOH and 0.5 M HCl. The solution rested for at least 24 h and then was filtered to remove any precipitates. Triplicate samples for initial $Fe(II)_{aq}$ concentration were taken. 15.0 mg of ^{56}Fe-oxide were added to 20 ml of ^{57}Fe(II) solution, and the solution was crimp-sealed with a Teflon-coated butyl rubber stopper. This high concentration of $Fe(II)_{aq}$ (~3 mM) and low solids concentration (0.75 g L^{-1}) were chosen in order to form Fe(III) oxidation products (after reaction with nitrobenzene) in amounts detectable by μ-XRD as determined in preliminary experiments. The solution was mixed end-over-end on a rotating disk for 1 h, and samples were taken in triplicate and filtered through a 0.45 μm syringe-tip filter to measure the $Fe(II)_{aq}$ concentration at this equilibration time. The amount of Fe(II) sorbed during the 1 h equilibration time ($Fe(II)_{sorb}$) was estimated as the difference between the initial and equilibrated $Fe(II)_{aq}$ concentrations. For selected experiments, the oxide particles were then filtered for Mössbauer analysis to characterize the ^{57}Fe(II) that sorbed and reacted with the ^{56}Fe-oxide during the 1 h uptake period only. In other experiments, the solution was spiked with the nitrobenzene compound and returned to agitation. Samples for nitrobenzene and its reduction products were taken periodically and filtered through 0.45 μm PTFE syringe-tip filters. The total amount of Fe(II) reacted at the end of the experiment ($Fe(II)_{reacted}$) was calculated as the difference between the initial and final $Fe(II)_{aq}$ concentrations.

After 23 h, final samples for $Fe(II)_{aq}$ (in triplicate) and nitrobenzene compounds were taken, and the final solution pH was measured. The Mops buffer was essential for maintaining some pH control during Fe(II) sorption, oxidation, and precipitation which cause significant release of H^+ (or consumption of OH^-). Abstaining from a buffer caused too great of a drop in pH and a cessation of the reactions, and periodic addition of NaOH solution for H^+ neutralization was not employed due to possible formation of unintended iron hydroxide precipitates at locally high OH^- concentrations. The solids were filtered onto a syringe-tip filter paper, and both were removed and preserved between two layers of oxygen-impermeable Kapton® tape for analysis with ^{57}Fe-Mössbauer spectroscopy and later μ-XRD.

2.4. Chemical analyses

Aqueous Fe(II) concentrations were measured by the ferrozine method (Stookey, 1970). The nitrobenzene compounds and their reduction products were measured by high pressure liquid chromatography using a C18 column, a 70/30 acetonitrile/water (containing ~0.1 mM ammonium acetate, pH 6), a 0.9 ml min^{-1} flowrate, and a UV–vis detector. The wavelengths of detection were 275 nm for 4-chloro-nitrobenzene, 235 nm for 4-chloro-phenylhydroxylamine and 4-chloro-aniline, 282 nm for 4-methyl-nitrobenzene, and 235 nm for 4-methyl-phenylhydroxylamine and 4-methyl-aniline (Klausen et al., 1995). The nitrobenzene and aniline compounds were quantified with respect to standard solutions, and concentrations of the intermediate phenylhydroxylamine was estimated at 235 nm using a mass balance approach when only 4-chloro-aniline was also present.

2.5. Mineral analyses

The specific surface area (SSA) of the ^{56}hematite rhombohedra, ^{56}goethite, and ^{56}magnetite were measured using N_2 adsorption by Brunauer–Emmett–Teller analysis. Measuring the SSA of ^{56}hematite needles and ^{56}maghemite was not possible due to the small amount of oxide synthesized. Therefore, the SSA of the ^{56}hematite needles was assumed to be similar to the SSA to their parent ^{56}goethite, and that of the ^{56}maghemite was assumed to be similar to that of their parent ^{56}magnetite. The measured SSA of ^{56}hematite hexagons was below the instrument detection limit (5 m^2 g^{-1}), so a geometric SSA was calculated assuming representative hexagonal particles 1 μm in size and 0.2 μm in thickness. Scanning electron microscopy images were collected with a LEO 1450 VP microscope and were used to estimate particle sizes and to observe changes in surface topology after heterogeneous Fe(II) oxidation experiments. Values for surface site densities were assumed from literature values reported for similar particle sizes and morphologies used here. SSA values, particle sizes, and surface site densities are summarized in Table 1.

μ-XRD patterns were collected with a Bruker D8 Discover μ-X-ray diffractometer with Co Kα radiation focused to a 300 μm spot size. Mössbauer spectra were collected with ^{57}Co radiation with linear acceleration in transmission mode. Sample temperatures were varied using a Janis® closed-cycle cryostat. Spectra were calibrated against a spectrum of α-Fe(0) foil. Recoil® software and Voigt-based models were used for spectral fitting.

3. RESULTS AND DISCUSSION

3.1. ^{57}Fe(II) uptake by ^{56}Fe oxides

Because the products of aqueous Fe(II) reactions with Fe-oxides alone must be distinguished from products resulting from oxidation by nitrobenzene, the fate of sorbed ^{57}Fe(II) was first characterized after a 1-h uptake period prior to any nitrobenzene addition. Prior studies already describe using Mössbauer spectroscopy the sorption and oxidation of ^{57}Fe(II) on ^{56}hematite (Williams and Scherer, 2004; Larese-Casanova and Scherer, 2007a; Rosso et al., 2010), ^{56}goethite (Williams and Scherer, 2004; Cwiertny et al., 2008), ^{56}magnetite (Gorski and Scherer, 2009),

Table 1
Physical properties of ^{56}Fe-oxide sorbents and abundances of ^{57}Fe-oxides formed within oxide suspensions of 0.75 g L^{-1}.

Oxide substrate[a]	Particle size[b]	SSA (m^2 g^{-1})	ρ_{site} sites[c] (nm^{-2})	Monolayer # sites[d]	During initial substrate growth		During secondary crystal growth		
					Detected ^{57}Fe phases	Stoichiometric ratio (slope)	Onset of 2° mineral (μmoles)		Stoichiometric ratio (slope)
							$Fe(II)_{reacted}$	# Monolayers	
^{56}Hematite rhombohedra	200 nm	10	2.6 (1)	3.9×10^{17}	Hematite	1.00	–	–	0.14
					Goethite	0.00	2.9	4.5	0.85
					Lepidocrocite	0.00	nd[e]	nd	0.01
^{56}Hematite hexagons	0.5–5 μm	4	2.3 (2)	1.3×10^{17}	Hematite	1.00	–	–	0.05
					Goethite	0.00	1.2	5.9	0.95
^{56}Hematite needles	500 nm	45	2.6 (1)	1.8×10^{18}	Hematite	1.00	–	–	0.75
					Goethite	0.00	13.2	4.5	0.25
^{56}Goethite	500 nm	45	1.7 (2)	1.1×10^{18}	Goethite	0.95	–	–	1.00
					Fe(II)	0.05	–	–	–
^{56}Magnetite	100 nm	85	5.0 (3)	6.4×10^{18}	Magnetite	1.00	–	–	0.75
					Lepidcrocite	0.00	46.8	4.4	0.25
^{56}Maghemite	100 nm	85	5.0 (4)	6.4×10^{18}	Magnetite	1.00	–	–	0.49
					Lepidocrocite	<1	40.9	3.9	0.51

[a] Fifteen milligrams of oxide substrate was added to each batch reactor.
[b] Values are approximated from viewing several primary particles within SEM images. Values refer to particle dimension of greatest length.
[c] Numbers in parentheses refer to the following references: 1, Jeon et al. (2004); 2, Pivovarov (1997); 3, Tamura et al. (1983); 4, Garcell et al. (1998).
[d] Number of surface sites within a batch reactor, calculated as mass of oxide × SSA × 10^{18} nm^2 m^{-2} × ρ_{site}.
[e] Not determined.

^{56}maghemite (Horio et al., 1994), ^{56}ferrihydrite (Williams and Scherer, 2004), and ferrihydrite of natural iron isotopic abundance (Silvester et al., 2005). Consistent with these reports, our results confirm the oxidation of ^{57}Fe(II) to ^{57}Fe(III) and assimilation of ^{57}Fe(III) into the ^{56}Fe-oxide structure within Fe-oxide suspensions of 3.0 mM ^{57}Fe(II) at pH 7.2.

^{57}Fe(II) was oxidized to ^{57}Fe(III) and formed ^{57}hematite on the ^{56}hematite rhombohedra, ^{56}hematite hexagons, and ^{56}hematite needles (Fig. 1). For most iron (hydr)oxides the Fe(III) oxidation state is distinguished from Fe(II) by their Mössbauer parameter values, with Fe(III) having a smaller center shift (0.3–0.6 mm s^{-1}) compared to Fe(II) (0.9–1.4 mm s^{-1}), and in the case of doublet signals, having a smaller quadrupole splitting distribution (0.5–1.0 mm s^{-1}) compared to Fe(II) (1.8–3.0 mm s^{-1}). Each ^{57}hematite formation exhibits a sextet pattern that is consistent with high spin, octahedral-coordinated Fe(III) in the presence of a hyperfine magnetic field (Murad and Cashion, 2004). The sextet patterns for the ^{56}hematite rhobohedra (at 4.2 K) and ^{56}hematite needles (at 77 K) were found to be composed of two sub-spectra sextets representing two distinct magnetic orders of hematite: the weakly ferromagnetic order and the antiferromagnetic order that are usually separated by the Morin transition temperature (T_M, ~265 K). As discussed previously for ^{57}Fe(II) uptake on ^{56}hematite (Larese-Casanova and Scherer, 2007a; Rosso et al., 2010), the coexistence of these two phases below T_M reveals a disruption of magnetic ordering within the formed ^{57}hematite caused by structural or electronic defects, possibly due to incomplete bonding formations for surface iron atoms, incorporation of H atoms into structural O linkages, or the rapid electron-hopping of donated valence electrons (Morrish, 1994; Dang et al., 1998; Kerisit and Rosso, 2006; Larese-Casanova and Scherer, 2007a; Rosso et al., 2010). Identification of the weakly ferromagnetic and antiferromagnetic phases was made by comparing modeled spectral parameters (center shift, quadrupole shift, and hyperfine field) to published values (Mössbauer spectral parameters for all experiments are listed in Table EA-1 in Electronic Annex 1). The weakly ferromagnetic order was not apparent within the ^{57}hematite formed on the ^{56}hematite hexagons due to the low absorption signal, and for simplicity this spectrum, as well as subsequent spectra for this oxide substrate, were modeled only with the antiferromagnetic order.

A ^{57}Fe(III)–goethite sextet pattern was readily apparent after ^{57}Fe(II) uptake on our ^{56}goethite (Fig. 1), similar to ^{57}Fe(II) oxidation on ^{56}goethite in previous reports (Williams and Scherer, 2004; Cwiertny et al., 2008; Amstaetter et al., 2010). Not all sorbed Fe(II) was oxidized, however, and an Fe(II) species was present among the filtered ^{56}goethite particles. A two-peak doublet coexisted with the formed ^{57}goethite sextet at 77 K and was consistent with a high-spin, octahedral coordinated Fe(II) species (Murad and Cashion, 2004) that has been observed after ^{57}Fe(II) uptake on aluminum oxide (Williams and Scherer, 2004; Larese-Casanova et al., 2010a,b), ^{56}hematite with high Fe(II) loading (Larese-Casanova and Scherer, 2007a), clay (Schaefer et al., 2011), and the same ^{56}goethite used in a separate study (Amstaetter et al., 2010). We attribute this Fe(II) doublet as either a collection of stable sorbed Fe(II) atoms or a surface hydroxide precipitate similar to ferrous hydroxide ($Fe(OH)_{2(s)}$) (Larese-Casanova and Scherer, 2007a) but not crystalline ferrous hydroxide (such as $Fe(OH)_{2(s)}$ that is homogenously-precipitated) which has a

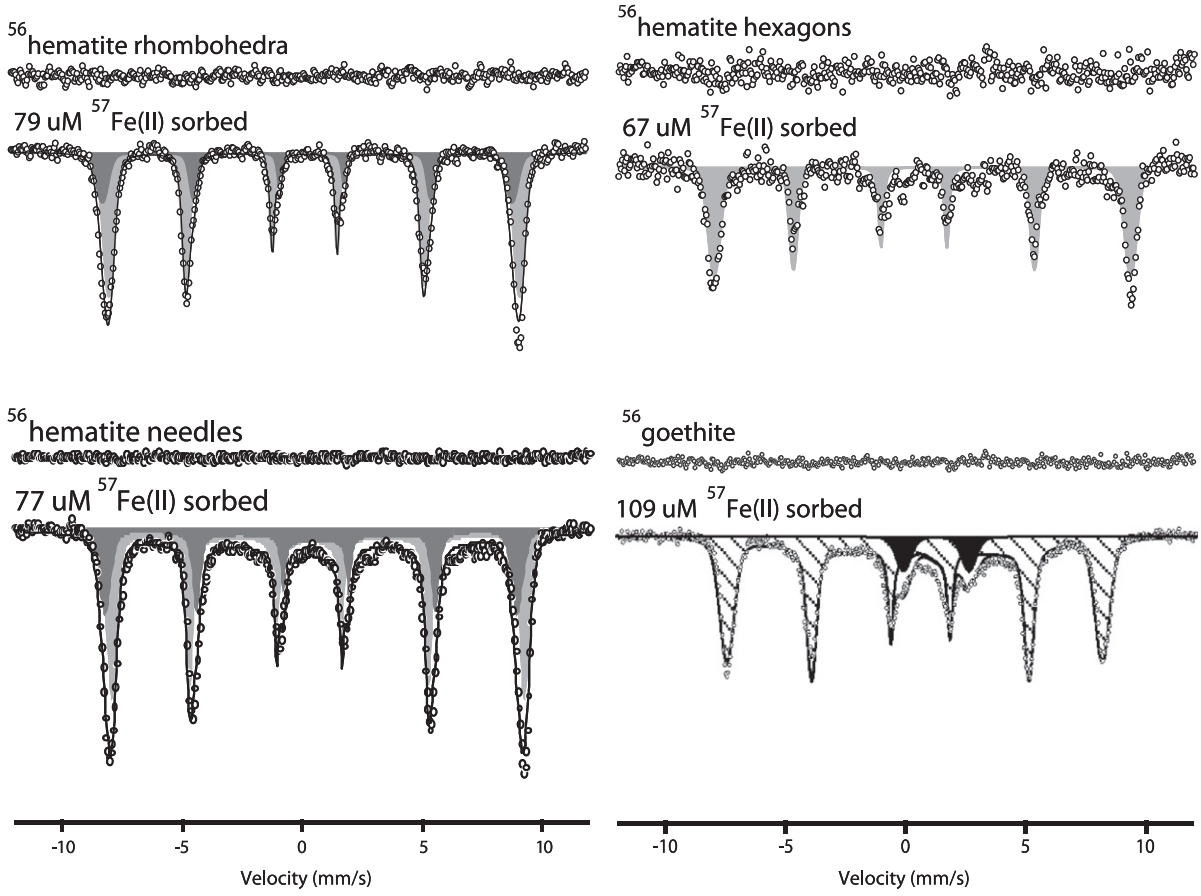

Fig. 1. ^{57}Fe-Mössbauer spectra of the three ^{56}hematite oxides and the ^{56}goethite before and after uptake of ^{57}Fe(II). Light gray sextets are hematite antiferromagnetic phases, dark gray sextets are hematite weakly ferromagnetic phases, the hatched sextet is goethite, and the black doublet is an Fe(II) species. The spectra for all ^{56}Fe oxides alone were collected at 4.2 K. The analysis temperatures for the ^{56}Fe oxides after ^{57}Fe(II) uptake were as follows: 4.2 K for ^{56}hematite rhombohedra, 4.2 K for ^{56}hematite hexagons, 77 K for ^{56}hematite needles, and 77 K for ^{56}goethite. Solution conditions and Mössbauer parameters are listed in Table EA-1 in Electronic Annex 1.

quadrupole splitting (peak spacing) far larger. The incomplete oxidation of sorbed Fe(II) on our ^{56}goethite further illustrates the notion that some iron oxides may have a limit to their ability to accept or store valence electrons from redox-active sorbates (Sherman, 1987; Rosso et al., 2003; Williams and Scherer, 2004; Kerisit and Rosso, 2006; Larese-Casanova and Scherer, 2007a; Yanina and Rosso, 2008). Surface Fe(II) accumulation ($Fe(II)_{surf}$) may be linked to surface site saturation, at least for hematite (Larese-Casanova and Scherer, 2007a). However, among the four oxide substrates within similar solution conditions in Fig. 1, no correlation exists between $Fe(II)_{surf}$ appearance and estimated site saturation: ^{56}goethite ($Fe(II)_{surf}$, at saturation), ^{56}hematite rhombohedra (no $Fe(II)_{surf}$, below saturation), ^{56}hematite hexagons (no $Fe(II)_{surf}$, above saturation), and ^{56}hematite needles (no $Fe(II)_{surf}$, below saturation). Moreover, this $Fe(II)_{surf}$ species has been observed to form after Fe(II) uptake on an identical ^{56}goethite (Amstaetter et al., 2010) although not on a similarly-prepared ^{56}goethite (Williams and Scherer, 2004) or on a ^{56}goethite of smaller particle size (Cwiertny et al., 2008). All four studies were conducted under fairly similar solution conditions, except that Amstaetter et al. (2010) and this work had higher dissolved Fe(II) concentrations (1.0–2.7 mM as opposed to 0.1–0.25) and lower pH (7.0–7.2 as opposed to 7.5–7.4) compared to the latter two publications. Reaction time and surface Fe(II) coverage does not explain $Fe(II)_{surf}$, either. The $Fe(II)_{surf}$ on goethite might be directed by a driving force from the higher dissolved Fe(II) or a pH sensitivity to interfacial electron transfer. In fact, a recent surface complexation model predicts that sorbed Fe(II) may be more resistant to oxidation by goethite at pH $\sim$ 7.0 compared to 7.5 (Hiemstra and van Riemsdijk, 2007). Additional sorption isotherms, surface charge descriptions, and spectroscopic data are needed to clarify this relationship among different substrate identities and morphologies. Finally, the $Fe(II)_{surf}$ is likely reactive to nitrobenzene, as no $Fe(II)_{surf}$ signal was observed in any spectra after nitrobenzene reduction (Section 3.2). This species may represent a collection of surface Fe(II) that, after its formation from dissolved Fe(II), is able to reduce a dissolved oxidant independently from dissolved Fe(II),

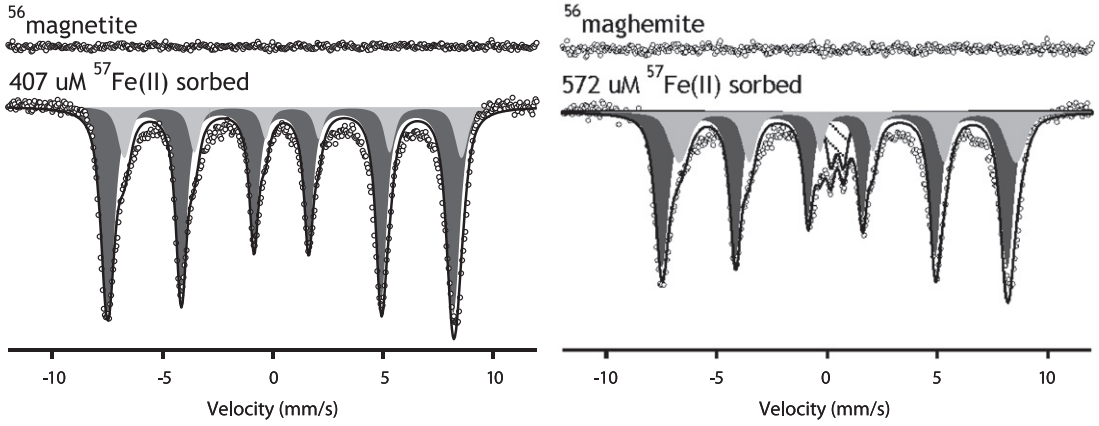

Fig. 2. ^{57}Fe-Mössbauer spectra of ^{56}magnetite and ^{56}maghemite before and after uptake of ^{57}Fe(II). The dark gray sextets are tetrahedral Fe(III) sites in magnetite. The light gray sextets are octahedral Fe(II)–Fe(III) sites in magnetite. The hatched doublet is lepidocrocite. The spectra for both ^{56}Fe oxides alone were collected at 4.2 K, and the spectra collected after ^{57}Fe(II) uptake were at 140 K. Solution conditions and Mössbauer parameters are listed in Table EA-1 in Electronic Annex 1.

which is necessary for most contaminant reduction with Fe(III) (hydr)oxides (Williams and Scherer, 2004).

^{56}Magnetite oxidized most of the sorbed ^{57}Fe(II) to form a ^{57}magnetite surface coating (Fig. 2) consistent with the observations of Gorski and Scherer (2009) (Gorski and Scherer, 2009). The two sextet subspectral patterns were apparent at 140 K and were typical for magnetite above its Verwey transition temperature (120 K): the sextet for tetrahedral Fe(III) A sites (which may contain overlapping area for unpaired B site Fe(III) (da Costa et al., 1995; Gorski and Scherer, 2009)), and the sextet for octahedral Fe(II)–Fe(III) B sites. The relative areas of the A (81%) and B (19%) sites for the formed ^{57}magnetite reveal a Fe(II):Fe(III) value of 0.09 which is less than the stoichiometric value of 0.50. The ^{56}magnetite substrate, also understoichiometric with regard to Fe(II) content prior to Fe(II) uptake (0.27), exerted an electron demand that was only partially satisfied by electrons transferred from sorbed ^{57}Fe(II) (based on the calculation procedure in Gorski and Scherer (2009)) into Fe(III) B sites.

^{57}Fe(II) uptake on ^{56}maghemite resulted in oxidation to Fe(III) of two forms: (i) a sextet pattern that most closely resembles magnetite rather than maghemite and (ii) a minor Fe(III) doublet pattern similar to lepidocrocite. The sextet pattern was deconvoluted as the two sub-spectra sextets representing the A and B sites of magnetite as described above. Fully distinguishing magnetite from maghemite within Mössbauer spectra is nearly impossible (Vandenberghe et al., 2000), leaving the possibility our interpreted magnetite sextets contains some maghemite. Nevertheless, the sextet subspectra for ^{57}Fe formed on the ^{56}maghemite are nearly identical to the sextet subspectra for ^{57}Fe formed on ^{56}magnetite as well as for synthetic magnetite (Fig. EA-2-1 in Electronic Annex 2). Our results are consistent with previous reports of magnetite formation on maghemite-like colloids after Fe(II) uptake at circumneutral pH (Tronc et al., 1984). Lepidocrocite formation was not expected and may be caused by rapid, collective Fe(II) oxidation at isolated locations that allowed Fe(III) to assemble into the γ-FeOOH structure instead of magnetite. For our purposes, we classify both the formed magnetite and lepidocrocite phases as "secondary" minerals because they differ from the parent (primary) maghemite sorbent.

The extent of Fe(II) uptake was checked for all subsequent experiments prior to the oxidant nitrobenzene addition and was found to be consistent with general trends for metal sorbates on metal oxide sorbents. Uptake extent was fairly constant within each preparation of ^{56}hematite and ^{56}goethite at pH 7.2 after 1 h (Fig. EA-2-2 in Electronic Annex 2). Fe(II) uptake was far greater (and much more variable) for ^{56}magnetite and ^{56}maghemite compared to the others and could be due to greater surface area, a possible lower pH_{pzc}, or a greater ability to accept and store valence electrons. Fe(II) uptake generally increased when pH increased from 7.0 to 7.8 for the ^{56}hematite rhombohedra, likely promoted by slight decreases in net surface charge typical of cation sorption to iron oxides.

Consistent with prior reports, Fe(II) oxidation after uptake was confirmed to result primarily in Fe(III) atoms that assumed the sorbent mineral structure and therefore identity on all Fe-oxide substrates with the exception of maghemite, which produced secondary phases. As discussed in the next section, further Fe(II) sorption and oxidation leads to additional formation of primary and secondary phases, and quantifying their proportions allows further characterization of the interfacial redox processes.

3.2. ^{57}Fe(II) uptake and oxidation during nitrobenzene reduction

Further heterogeneous oxidation of ^{57}Fe(II) on the ^{56}Fe-oxide surfaces was promoted by the reaction with a dissolved nitrobenzene compound that served as an oxidizing agent. To first establish an "endpoint" of maximum ^{57}Fe surface accumulation on each oxide, nearly all 3.0 mM ^{57}Fe(II) was oxidized with about 450 μM 4-chloro-nitrobenzene within identical solution conditions (pH 7.2, 30 mM Mops, 30 mM NaCl). Reduction of 4-chloro-nitro-

benzene to 4-chloro-aniline (with the transient appearance of the intermediate 4-chloro-phenolhydroxylamine) was observed only when aqueous ^{57}Fe(II) was present with any ^{56}Fe-oxide (Fig. 3 provides one example with ^{56}hematite rhombohedra). No nitrobenzene reduction was observed in aqueous Fe(II) solutions without an iron oxide (data not shown) confirming that the electrons provided for the reduction stemmed from mineral bound Fe(II). Heterogeneous nitrobenzene reduction by Fe(II) and iron oxides is usually rapid (Klausen et al., 1995), and here nitrobenzene reduction was nearly complete within 0.5–3 h. Rates of nitrobenzene reduction could be described with a pseudo-first order kinetic model (Table EA-1 in Electronic Annex 1 lists rate coefficients k for all solutions), but only for early timepoints where aqueous Fe(II) concentrations changed little. The reaction rate deviated from first-order toward the end of the reaction due to depletion of aqueous Fe(II) concentrations or due to a change in surface Fe-oxide identity (data not shown). The initial rates did not show any appreciable trend with respect to initial 4-chloro-nitrobenzene concentration (Fig. EA-2-3 in Electronic Annex 2) or solution pH (Fig. EA-2-4 in Electronic Annex 2).

Concomitant loss of aqueous Fe(II) at the termination of the reaction was documented (Table EA-1 in Electronic Annex 1) and indicates the dissolved Fe had become associated with the solid phase. In most experiments, the amount of aqueous Fe(II) lost was more than sufficient to account for the observed aniline formation (the stoichiometry is six electrons transferred from Fe(II) for each aniline formed). An often-used reference point for metal deposition is monolayer coverage; in these and subsequent experiments, we deposited a far greater number of theoretical ^{57}Fe-monolayers (range of less than one to greater than 300, Table EA-1 in Electronic Annex 1) by using high aqueous Fe(II) concentration (3.0 mM) and a low oxide concentration (0.75 g L^{-1}) compared to other experiments in the literature that focused primarily on contaminant transformation kinetics instead of iron crystal growth (e.g., Buchholz et al., 2011). The high amount of Fe deposition allows for observing surface topology transformations with scanning electron microscopy and to confirm secondary iron mineral identity using μ-X-ray diffraction in addition to ^{57}Fe-Mössbauer spectroscopy.

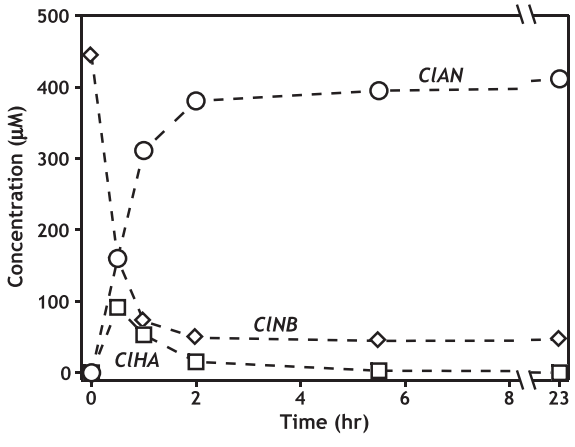

Fig. 3. 4-Chloro-nitrobenzene (ClNB) reduction, 4-chloro-hydroxylamine (ClHA), 4-chloro-aniline (ClAN) in the presence of ^{56}hematite rhombohedra. Oxide loading was 0.75 g L^{-1}, solution pH was 7.2. Other solution conditions for this batch reactor (#8) appear in Table EA-1 in Electronic Annex 1.

3.2.1. ^{56}Hematite and ^{56}goethite substrates

Heterogeneous Fe(II) oxidation driven by nitrobenzene reduction resulted in the growth of the underlying hematite substrate and the formation of secondary Fe-oxide phases on all three hematite substrates (Fig. 4). Goethite was the most abundant ^{57}Fe-oxide formed on the ^{56}hematite rhombohedra and hexagons, but only a minor amount appeared on the ^{56}hematite needles. Goethite is readily distinguished from hematite in Mössbauer spectra based on its characteristic quadrupole shift value (about -0.12 mm s^{-1}) and its lower hyperfine magnetic field (<50 T for goethite, >52 T for hematite at temperatures 77 K and below). Goethite reflections were also detected within μ-XRD patterns, most noticeably the 24.5° and 42.6° 2Θ reflections, for the rhombohedra and hexagon substrates. While a minor lepidocrocite signal (1% abundance in the Mössbauer spectrum) was observed with ^{56}hematite rhombohedra the small amount of goethite formed on the ^{56}hematite needles was not visible in XRD. For similar iron oxide surface investigations in the future, additional techniques such as diffuse reflectance spectroscopy may provide more sensitive identification and quantification of primary and secondary iron oxides, in particular hematite and goethite (da Costa et al., 2009).

Acicular shapes (needle-like) similar to goethite were readily apparent on the hexagon surfaces within SEM images (Fig. 6). Rhombohedra surfaces became roughened with small stubs which we attribute to goethite, and no changes in surface features were observable for the ^{56}hematite needles. The appearance of goethite indicates that, at some point during Fe(II) oxidation, newly-formed Fe(III) preferably nucleated as α-FeOOH instead of α-Fe_2O_3, which is conceivable considering goethite is one Fe-oxide phase that can form via Fe(II) oxidation whereas hematite usually forms via a dehydration mechanism or under hydrothermal conditions (Cornell and Schwertmann, 2003). However, extensive growth of hematite surface deposits is possible via Fe(II) oxidation by underlying hematite during far slower reaction rates (Rosso et al., 2010), so the formation of goethite observed here might be due to the rapid Fe(II) oxidation in which Fe(III) production was too fast to properly assimilate as hematite. Nevertheless, in order for well-defined goethite crystals to grow (at least on the ^{56}hematite hexagons), the reactive surface for Fe(II) sorption and oxidation likely transitioned from the hematite surface to goethite nuclei on which Fe(III) further accumulated as α-FeOOH. Indeed, when ^{56}goethite was provided as the parent Fe-oxide substrate, only ^{57}goethite was observed to form in Mössbauer spectra (Fig. 4), and goethite crystal lengthening has been observed within TEM images after heterogeneous oxidation by nitrobenzene reduction (Chun et al., 2006).

The greater preference for goethite formation over lepidocrocite on hematite may be caused by the hematite surface providing a template for epitaxial growth of goethite. Oriented crystal growth of goethite needles on

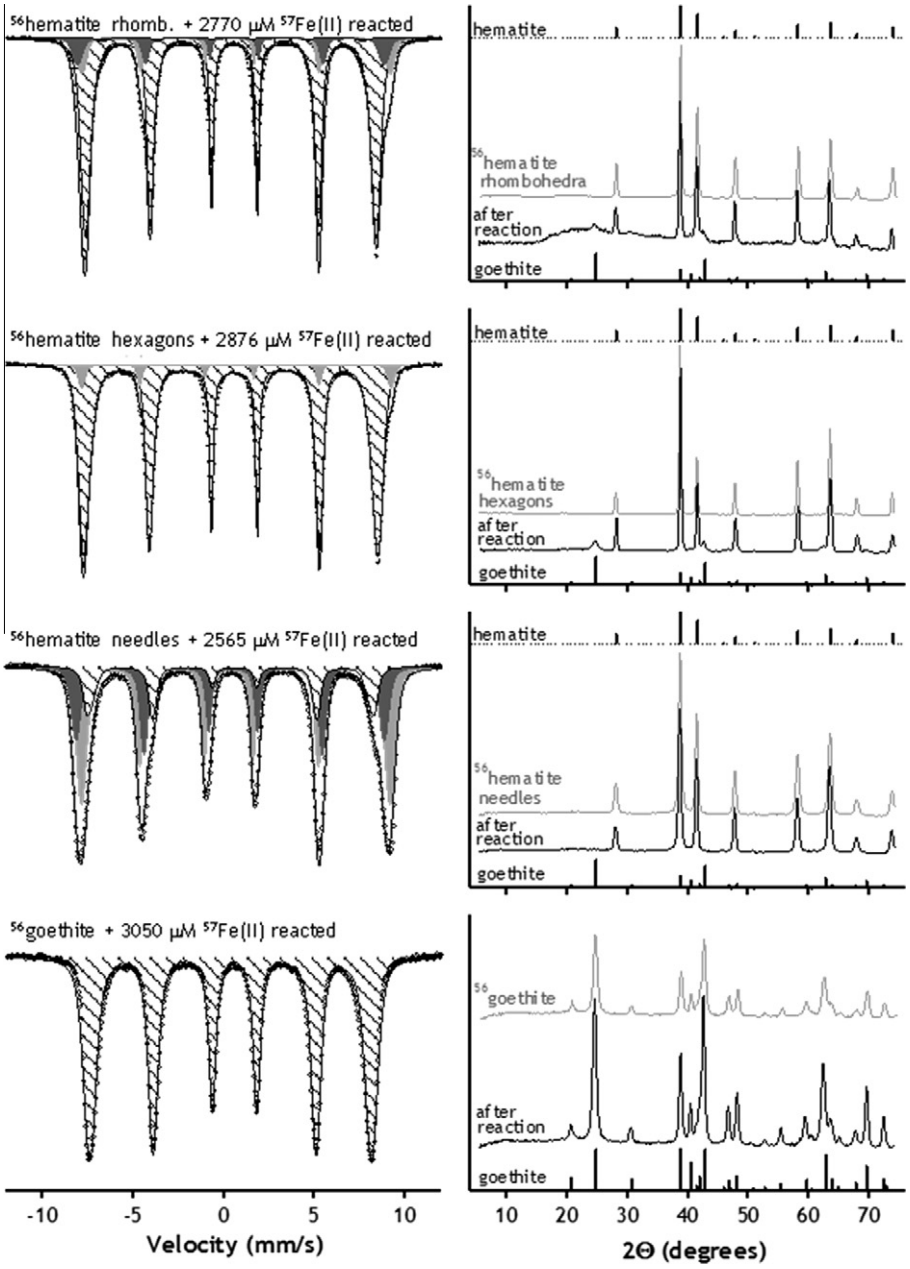

Fig. 4. ^{57}Fe-Mössbauer spectra of ^{57}Fe-oxides formed (left column) and μ-XRD patterns of total oxides (right column) after sorption and oxidation of ^{57}Fe(II) by 4-chloro-nitrobenzene on the three ^{56}hematites and ^{56}goethite. Light gray sextets are hematite antiferromagnetic phases, dark gray sextets are hematite weakly ferromagnetic phases, and the hatched sextet is goethite. The spectrum with ^{56}hematite rhombohedra contains a miniscule lepidocrocite sextet unnoticeable at this scale. The Mössbauer analysis temperatures were as follows: 4.2 K for ^{56}hematite rhombohedra, 4.2 K for ^{56}hematite hexagons, 77 K for ^{56}hematite needles, and 77 K for ^{56}goethite. Solution conditions and Mössbauer parameters are listed in Table EA-1 in Electronic Annex 1. All ^{57}Fe-oxides were confirmed at other analysis temperatures, but the clearest spectra are shown here.

the hematite hexagonal plates may be favored by the crystal geometries of goethite and hematite with the long axis of some goethite needles arranged parallel to each other and projecting from edges of the hematite plates (Fig. 6; and additional image in Fig. EA-2-5 in Electronic Annex 2). Others have reported oriented crystal growth of goethite on hematite and suggested epitaxy may result from the hexagonal close-packed oxygen packing arrays line up for the two Fe-oxides, where the interplanar spacings reasonably match among certain crystallographic faces, resulting in projections of goethite needles oriented 60° of each other but in the same plane (Atkinson et al., 1968; Barron et al., 1997). Some goethite needles in our images are arranged in similar geometry.

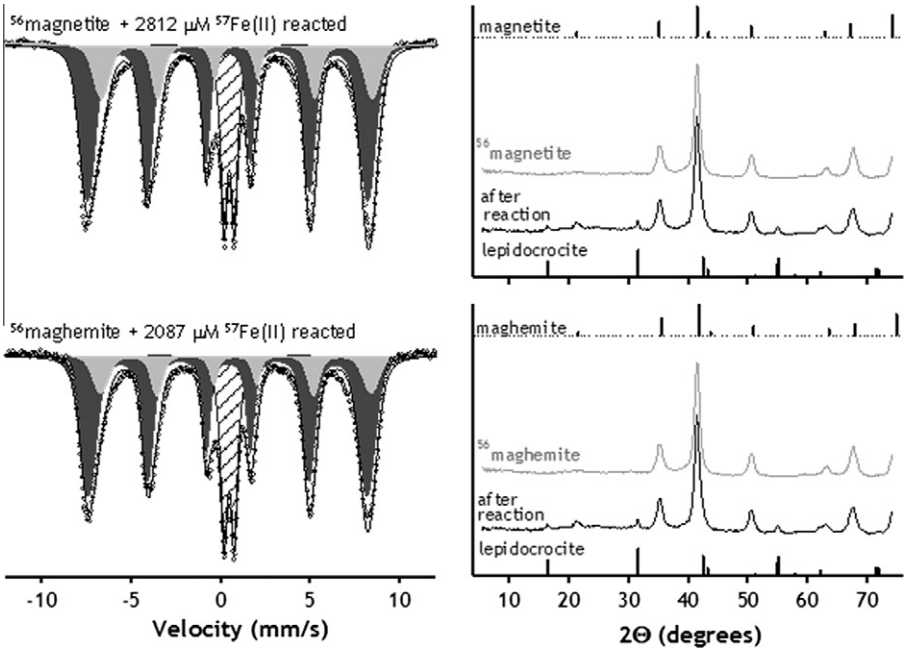

Fig. 5. ^{57}Fe-Mössbauer spectra of ^{57}Fe phases formed (left column) and μ-XRD patterns of total oxides (right column) after sorption and oxidation of ^{57}Fe(II) by nitrobenzene on ^{56}magnetite and ^{56}maghemite. The dark gray sextets are tetrahedral Fe(III) sites in magnetite. The light gray sextets are octahedral Fe(II)–Fe(III) sites in magnetite. The hatched doublet is lepidocrocite. The Mössbauer analysis temperatures were 140 K. Solution conditions are listed in Table EA-1. Mössbauer parameters are listed in Table EA-2.

3.2.2. ^{56}Magnetite and ^{56}maghemite substrates

Heterogenous Fe(II) oxidation driven by nitrobenzene reduction resulted in prominent magnetite growth and the formation of lepidocrocite on both the ^{56}magnetite and ^{56}maghemite substrates (Fig. 5). ^{57}Magnetite is indicated in the Mössbauer spectra as a sextet pattern identical to the one formed after ^{57}Fe(II) uptake alone. Lepidocrocite was readily distinguished from the magnetite signal at 140 K based on its paramagnetic doublet whose model parameters are similar to synthesized lepidocrocite and dissimilar to ferrihydrite and superparamagnetic goethite (Table EA-2 in Electronic Annex 2). Lepidocrocite was confirmed within μ-XRD patterns, notably at 17.0°, 31.7°, and 55.7° 2Θ reflections.

Note that lepidocrocite formation also occurs via homogeneous Fe(II) oxidation with O_2 at circumneutral pH but not on hematite (where goethite was formed as secondary phase) suggesting that magnetite and maghemite likely do not possess a template effect for epitaxal growth or goethite formation. Unlike ^{56}hematite, the ^{56}magnetite and ^{56}maghemite did not appear to support oriented Fe-oxide growth (Fig. 6). Instead, the acicular needle formations, presumed to be lepidocrocite, often assume a spherulite morphology with several needles projecting from a common center (another image is provided as Fig. EA-2-6 in Electronic Annex 2). Spherulites of lepidocrocite may form during fast Fe(II) oxidation kinetics (Cornell and Schwertmann, 2003), although the more familiar lathe morphologies are typical for Fe(II) oxidation by O_2. Spherulites suggest lepidocrocite nucleated on the Fe-oxides and became the preferred surface for continued Fe(II) sorption and oxidation and Fe(III) accumulation.

3.3. Controls on ^{57}Fe product formation

The Mössbauer spectra from Figs. 4 and 5 reveal that both the processes of Fe-oxide substrate growth and secondary Fe-oxide formation may occur during extensive Fe(II) oxidation on hematite, magnetite, and maghemite. But the different proportions of secondary Fe-oxide formation for each substrate highlight the need to understand the relative occurrence of each process. A second suite of experiments were conducted to trace the onset of secondary Fe-oxide formation and to test the geochemical solution conditions that may govern their formation. Progressive Fe(II) oxidation and Fe(III) accumulation was achieved with varying additions of 4-chloro-nitrobenzene to otherwise identical suspensions (with respect to Fe(II) added and pH) of each ^{56}Fe-oxide. Abundances of each ^{57}Fe-oxide formed were estimated from the relative Mössbauer spectral area by the following equation:

$$\mu\text{moles phase}_i = (\%\ \text{spectral area phase}_i) \times (\text{total } \mu\text{moles Fe(II)}_{aq}\ \text{reacted})$$

where i = hematite, goethite, lepidocrocite, or magnetite, and the term 'reacted' refers to the amount of Fe(II) removed from the aqueous phase and reacted in some form with the solid phase. The percent spectral area is assumed to be equivalent to percent abundance, and all phases were assumed to have similar recoilless fractions. Solution conditions, Mössbauer model parameters, phase abundances, and initial nitrobenzene reduction rates for all conditions are summarized in Table EA-1 in Electronic Annex 1.

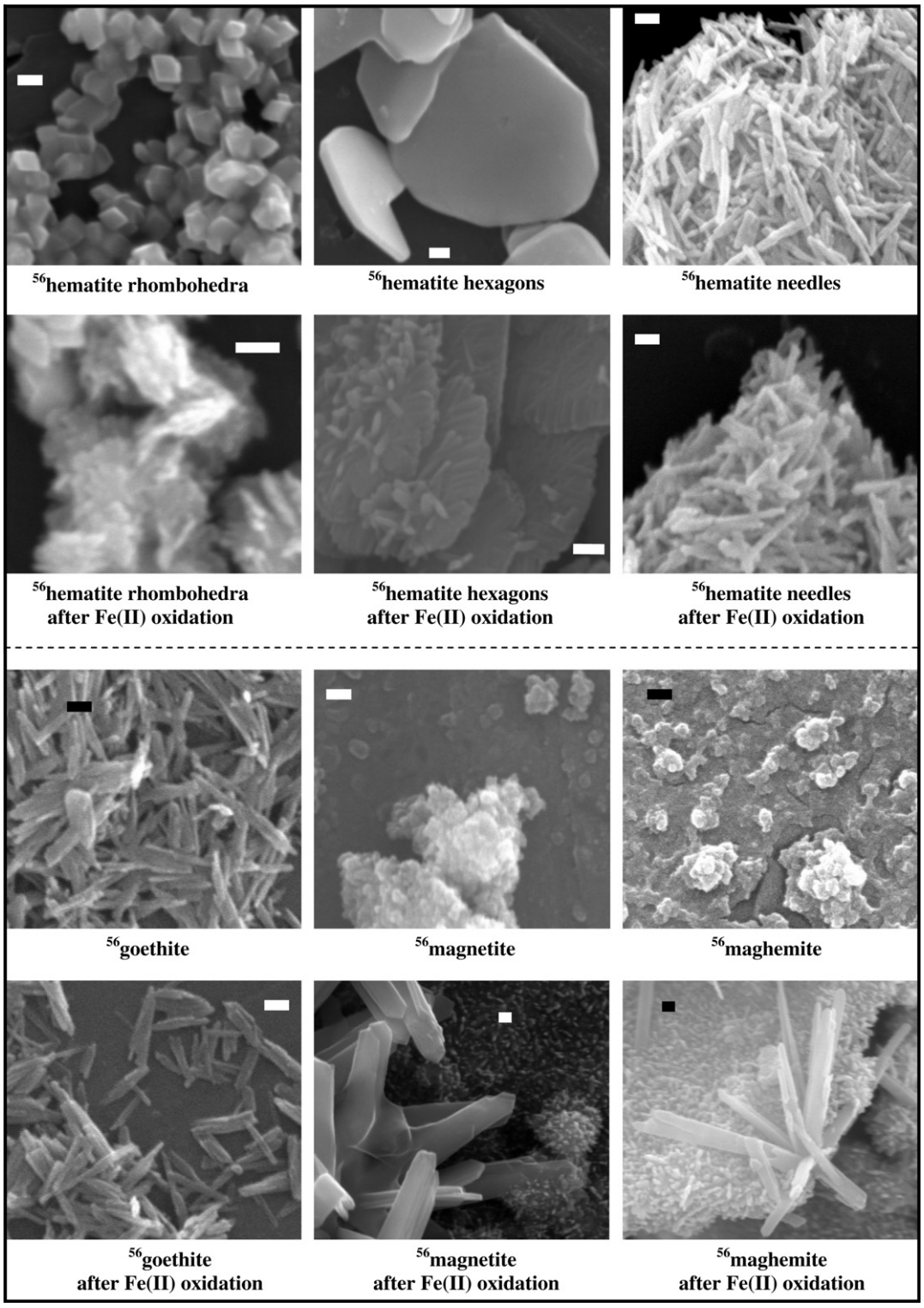

Fig. 6. Scanning electron microscope images of iron oxides before and after sorption and oxidation of ^{57}Fe(II) by driven by nitrobenzene reduction. Scale bars are 200 nm for all images.

^{57}Fe(II) oxidation on ^{56}hematite rhombohedra resulted in growth of ^{57}hematite, ^{57}goethite, and ^{57}lepidocrocite, with ^{57}goethite the predominating form for most solution conditions. For the rhombohedra only, several geochemical solution parameters were varied to test their influence on the ^{57}Fe-oxide abundances including solution pH (7.0–7.8), buffer concentration (1–80 mM Mops), Fe(II) uptake pre-equilibration time (1 vs. 24 h), and Fe(II) oxidation rate

(as controlled by the substitution of nitrobenzene, i.e., 4-chloro-nitrobenzene vs. 4-methyl-nitrobenzene), in addition to the extent of Fe(II) oxidation (oxide loading remained constant at 0.75 g L^{-1}). The abundance of the secondary ^{57}goethite and ^{57}lepidocrocite did not correlate with any solution-phase parameter listed above. Instead, the abundance of ^{57}goethite correlated well with the amount of Fe(II) oxidized only (Fig. 7). This indicates that the major control on ^{57}goethite formation is the ^{56}hematite rhombohedra itself, and the solution parameters above assert only minor influences.

The plot of ^{57}goethite abundance with respect to the amount of aqueous Fe(II) reacted (Fig. 7A) can be interpreted as providing an apparent stoichiometry. The slope of the regression line for ^{57}goethite (0.85) indicates that, once ^{57}goethite nucleates on the ^{56}hematite surface, 85% of ^{57}Fe(II) reacted will assemble as ^{57}goethite, with the remaining ^{57}Fe as ^{57}hematite or a minor amount of ^{57}lepidocrocite. If the ^{56}hematite substrate truly controls ^{57}Fe(III) product formation, the same linear relationship, but with different slopes, should be exhibited by the other two ^{56}hematites. Indeed, good linear fits provide slopes of 0.95 for ^{56}hematite hexagons (Fig. 7B) and 0.25 for ^{56}hematite needles (Fig. 7C).

The different proportions of ^{57}goethite growth on the three ^{56}hematite morphologies (as indicated by the different slopes in Fig. 7) should be controlled by a physical or electronic property of the hematite, such as specific surface area, total surface sites, site density, particle volume, aggregate size, electron conducting ability, or a combination of these properties as they are all interrelated. The approximated number of total surface sites, calculated from measured specific surface area and assumed site density (Table 1), serves as the best property related to surface Fe(III) accumulation and in fact correlates well with the ^{57}goethite and ^{57}hematite stoichiometric values (Fig. 7D).

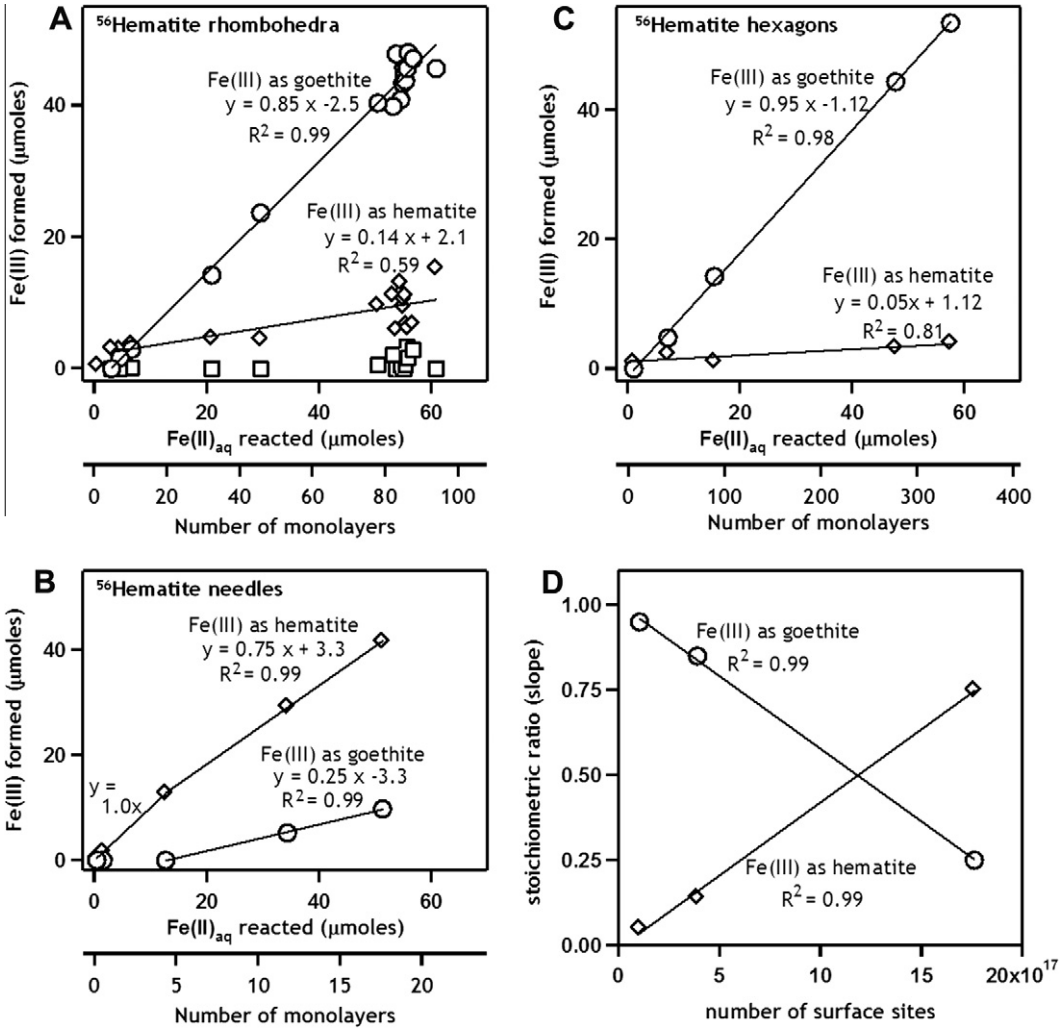

Fig. 7. Amount of reacted Fe(II) partitioned to each ^{57}Fe phase detected within Mössbauer spectra ("Fe(III) formed") with respect to the amount of aqueous Fe(II) reacted for the three hematite substrates: rhombohedra (A), hexagons (B), and needles (C). Plot (D) is a graph of slope values for the regression lines after the onset of goethite formation with respect to an estimated number of surface sites available within the batch reactors. Diamonds represent hematite, circles represent goethite, and squares represent lepidocrocite. The amount of Fe(III) formed was determined referring to spectra collected at 77 K.

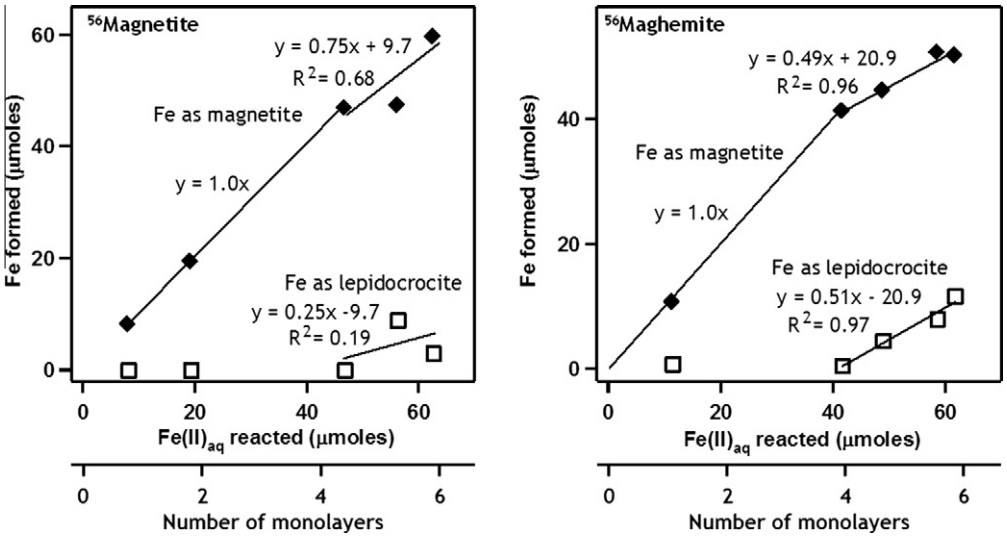

Fig. 8. Amount of reacted Fe(II) partitioned to each ^{57}Fe phase detected within Mössbauer spectra ("Fe(III) formed") with respect to the amount of aqueous Fe(II) reacted for the magnetite and maghemite substrates. Closed diamonds represent magnetite, and open squares represent lepidocrocite. The amount of Fe(III) formed was determined referring to spectra collected at 140 K.

A greater number of available surface sites allows more opportunity for the underlying hematite substrate to assimilate Fe(III) into the hematite structure for a given amount of Fe(II) oxidized. Conversely, if a lower amount of surface sites is available, Fe(III) assimilation as hematite may become exhausted sooner, and subsequent Fe(III) acquisition may be "forced" into secondary Fe-oxide formation. This interpretation suggests that there is a limit to the amount of Fe(III) assimilated as hematite prior to secondary goethite formation. In fact, the onset of ^{57}goethite growth does coincide among the three hematite morphologies. The *x*-intercept of the linear regression lines in Fig. 7A–C indicates goethite first appears after about four monolayers of Fe(III) coverage for all three hematites of different specific surface area. These coincidences of goethite onset indicate that the initiation of secondary goethite growth is governed primarily by surface availability rather than electronic or volumetric properties.

Nevertheless, while bulk surface availability may be a driving factor for goethite formation on hematite, the specific molecular description of surface precipitation is still in need and may be achievable in future studies using surface complexation models and face-specific site geometry and reactivity. Other studies have closely examined Fe(II) sorption and oxidation processes on other metal oxides using the charge distribution model while considering reactive site availability and surface molecular configurations for different mineral faces (Hiemstra and van Riemsdijk, 2007). The specific reactivities of different hematite faces with respect to dissolution and precipitation (Yanina and Rosso, 2008) and electron transfer (Kerisit and Rosso, 2006) have been noted. The Fe(III) accumulation after surface Fe(II) oxidation likely does not occur on hematite as a uniform, multi-layer coverage considering the different electron transfer rates among different hematite faces, proximities to those surfaces, and surface sites (Yanina and Rosso, 2008). Rather, specific hematite faces may have higher propensities for Fe(II) sorption and oxidation driven by an external oxidant and may play a role in specific secondary goethite formation. The close matching of goethite geometry to the hematite (0 0 1) face (Barron et al., 1997), and any other examples of epitaxy on iron oxide substrates, supports the idea that specific surfaces may direct Fe(III) accumulation into a secondary mineral. Modeling approaches similar to Hiemstra and van Riemsdijk (2007) need to be conducted considering multi-layer Fe(III) accumulation on multiple hematite faces in order to better account for the physical arrangement of atoms during secondary crystal growth. Finally, the role of hematite micropores in Fe(II) sorption and oxidation requires further attention. While our BET surface area measurements did not include micropore analysis, there is a possibility of sub-nanometer sized pores existing on hematite surfaces (particularly for hydrothermally-synthesized hematite from goethite, i.e., the hexagons (Naono et al., 1987)), providing additional surface area, and lessening the number of monolayer coverages. A clearer conceptual model can be made by combining our observations of secondary mineral formation with additional X-ray and infra-red based surface spectroscopic techniques as well as surface porosity analysis.

The onset of lepidocrocite growth also occurred after approximately four monolayer coverage on ^{56}magnetite and ^{56}maghemite (Fig. 8) (neglecting the minor amount of ^{57}lepidocrocite formed on maghemite after ^{57}Fe(II) oxidation alone). Compared to the ^{56}hematites, far greater ^{57}Fe(II) sorption and oxidation was required until lepidocrocite formation likely due to the much higher surface area of these oxides (Table 1). Altogether, the coincidence of ^{57}lepidocrocite and ^{57}goethite formation on their respective ^{56}Fe-oxides may point to a common feature—namely, available surface area—that controls Fe(III) surface assimilation among hematite, magnetite, and maghemite. However, the electronic properties of magnetite and maghemite should also be important factors because these oxides

possess a large capacity for valence electron acceptance from sorbed Fe(II) when the oxide Fe(II) content is understoichiometric (Gorski and Scherer, 2009).

3.4. Implications for Fe(II) uptake and contaminant reduction

The precise mechanisms of electron transfer from sorbed Fe(II) to a sorbed contaminant remains unknown, whether directly from sorbed Fe(II) atoms or through the Fe-oxide structure. Considering that a large fraction of sorbed Fe(II) is transient under most geochemical conditions (Williams and Scherer, 2004; Larese-Casanova and Scherer, 2007a; Cwiertny et al., 2008; Gorski and Scherer, 2009) and that Fe-oxides' semiconducting ability allows for some electron storage and transfer, the eventual electron transfer route from sorbed Fe(II) to the sorbed contaminant may very well pass through portions of the Fe-oxide structure. Park and Dempsey (2005) (Park and Dempsey, 2005) provide a reaction model in support of this pathway. Here, we observe the same Fe(III) product (^{57}hematite) whether sorbed Fe(II) is oxidized by hematite alone (cf. Section 3.1) or sorbed Fe(II) oxidation is promoted by low concentrations of nitrobenzene, which suggests the Fe(II) oxidation pathway (that is, electron transfer to the underlying hematite) may be the same for both cases. More sophisticated experiments are needed to further distinguish and characterize the two electron transfer pathways.

The nucleation of goethite and lepidocrocite is expected to require a localized cluster of Fe(III)-hydroxide polymers, which in turn implies localized spots of high Fe(II) sorption and oxidation. These results are consistent with the model proposed by Park and Dempsey (2005) and the surface images provided by Yanina and Rosso (2008) which show face-specific oxidative deposition of Fe.

Available surface area is an important parameter for the extent of Fe(II) uptake on metal oxides and contaminant reduction rates, with greater extent of Fe(II) uptake or faster reduction kinetics observed for greater concentrations of reactive surface sites in solution (e.g., Amonette et al., 2000; Strathmann and Stone, 2003). Available surface area also appears to be related to the assimilative capacity for newly-formed Fe(III). Accumulation of Fe(III) beyond this capacity may indeed result in the formation of new Fe-oxides and a remodeling of the surface topology (Pecher et al., 2002) which may affect contaminant reduction rates favorably or unfavorably (Klupinski et al., 2004; Chun et al., 2006). Our observation of goethite growth on hematite substrates may provide the reason for a recent observation of a ^{13}C kinetic isotope enrichment value for CCl_4 that changed during reaction with Fe(II) on a hematite surface (Zwank et al., 2005); the enrichment value had changed to resemble one of CCl_4 reaction with Fe(II) and goethite after prolonged reaction with the hematite surface. Additional studies are needed to examine Fe(III) assimilation capacity and secondary Fe-oxide formation for other $Fe(II)_{aq}$:Fe-oxide ratios and for other heterogeneous contaminant reduction rates in order to develop a more robust interpretation of Fe(III) surface accumulation.

4. CONCLUSIONS

Heterogeneous Fe(II) oxidation on Fe-oxides results in Fe(III) production which may be assimilated as part of the underlying Fe-oxide structure or may form secondary Fe-oxides. The identity of secondary Fe-oxides depends on the identity of the underlying Fe-oxide: goethite formed on hematite of three morphologies, and lepidocrocite formed on magnetite and maghemite. A fairly narrow range of circumneutral solution pH, buffer concentration, and equilibration time had little influence on Fe(III) product distribution. Because lepidocrocite is expected to be the only Fe(III) oxide formed by homogeneous Fe(II) oxidation by O_2, the nucleation and precipitation of goethite needles in regular 60° orientations on hematite surfaces indicates hematite may act as a template for goethite formation by heterogeneous Fe(II) oxidation.

The initiation of secondary Fe-oxide formation occurred after 4–6 equivalents of monolayer coverage of the supporting mineral. The available surface area, or sites, appears to control the initiation of secondary Fe-oxide formation. The proportion of goethite formation on the three hematites was linked to number of surface sites, and the onset of secondary Fe-oxide formation was linked to surface area via the 4–6 monolayer coverage limit. Overall, extensive Fe(II) sorption and oxidation results in surface remodeling and formation of new iron phases. The full implications to contaminant reduction rates, iron biogeochemical cycling, and surface sorption processes require further study.

ACKNOWLEDGMENTS

The authors thank Katja Amstätter, Inga Köhler, Christoph Berthold for assistance with micro-X-ray diffraction; Nikolas Hagemann and Hartmut Schultz for assistance with scanning electron microscopy; and Elmar Ritter for assistance with the hydrothermal synthesis of the hematite hexagons. We also thank Christian Schröder and the anonymous reviewers for their comments which improved the manuscript. Funding was provided by the German Research Foundation (Deutsche Forschungsgemeinschaft) through Grant HA 3453/5-1.

APPENDIX A. SUPPLEMENTARY DATA

Supplementary data associated with this article can be found, in the online version, at http://dx.doi.org/10.1016/j.gca.2012.05.031.

REFERENCES

Amonette J. E., Workman D. J., Kennedy D. W., Fruchter J. S. and Gorby Y. A. (2000) Dechlorination of carbon tetrachloride by Fe(II) associated with goethite. *Environ. Sci. Technol.* **34**, 4606–4613.

Amstaetter K., Borch T., Larese-Casanova P. and Kappler A. (2010) Redox transformation of arsenic by Fe(II)-activated goethite (a-FeOOH). *Environ. Sci. Technol.* **44**, 102–108.

Atkinson R. J., Posner A. M. and Quirk J. P. (1968) Crystal nucleation in Fe(III) solutions and hydroxide gels. *J. Inorg. Nucl. Chem.* **30**, 2371–2374, IN1–IN2, 2375–2381.

Barron V., Galvez N., Hochella M. F. and Torrent J. (1997) Epitaxial overgrowth of goethite on hematite synthesized in phosphate media: a scanning force and transmission electron microscopy study. *Am. Mineral.* **82**, 1091–1100.

Borch T., Kretzschmar R., Kappler A., Van Cappellen P., Binder-Vogel M., Voegelin A. and Campbell K. (2010) Biogeochemical redox processes and their impact on contaminant dynamics. *Environ. Sci. Technol.* **44**, 15–23.

Buchholz A., Laskov C. and Haderlein S. B. (2011) Effects of zwitterionic buffers on sorption of ferrous iron at goethite and its oxidation by CCl_4. *Environ. Sci. Technol.* **45**, 3355–3360.

Buerge I. J. and Hug S. J. (1999) Influence of mineral surfaces on chromium(VI) reduction by iron(II). *Environ. Sci. Technol.* **33**, 4285–4291.

Catalano J. G., Fenter P., Park C., Zhang Z. and Rosso K. M. (2010) Structure and oxidation state of hematite surfaces reacted with aqueous Fe(II) at acidic and neutral pH. *Geochim. Cosmochim. Acta* **74**, 1498–1512.

Charlet L., Silvester E. and Liger E. (1998) N-compound reduction and actinide immobilisation in surficial fluids by Fe(II): the surface $Fe(III)OFe(II)OH^0$ species as major reductant. *Chem. Geol.* **151**, 85–93.

Charlet L., Bosbach D. and Peretyazhko T. (2002) Natural attenuation of TCE, As, Hg linked to the heterogeneous oxidation of Fe(II): an AFM study. *Chem. Geol.* **190**, 303–319.

Chun C. L., Penn R. L. and Arnold W. A. (2006) Kinetic and microscopic studies of reductive transformations of organic contaminants on goethite. *Environ. Sci. Technol.* **40**, 3299–3304.

Cornell R. M. and Schwertmann U. (2003) *The Iron Oxides: Structure, Properties, Reactions, Occurrences and Uses*. Wiley-VCH, Weinheim.

Crosby H. A., Johnson C. M., Roden E. E. and Beard B. L. (2005) Coupled Fe(II)–Fe(III) electron and atom exchange as a mechanism for Fe isotope fractionation during dissimilatory iron oxide reduction. *Environ. Sci. Technol.* **39**, 6698–6704.

Cwiertny D. M., Handler R. M., Schaefer M. V., Grassian V. H. and Scherer M. M. (2008) Interpreting nanoscale size-effects in aggregated Fe-oxide suspensions: reaction of Fe(II) with goethite. *Geochim. Cosmochim. Acta* **72**, 1365–1380.

da Costa G. M., De Grave E., de Bakker P. M. A. and Vandenberghe R. E. (1995) Influence of nonstoichiometry and presence of maghemite on the Moessbauer spectrum of magnetite. *Clays Clay Miner.* **43**, 656–668.

da Costa G. M., Barrón V., Mendonça Ferreira C. and Torrent J. (2009) The use of diffuse reflectance spectroscopy for the characterization of iron ores. *Miner. Eng.* **22**, 1245–1250.

Dang M. Z., Rancourt D. G., Dutrizac J. E., Lamarche G. and Provencher R. (1998) Interplay of surface conditions, particle size, stoichiometry, cell parameters, and magnetism in synthetic hematite-like materials. *Hyperfine Interact.* **117**, 271–319.

Duvigneaud P. H. and Derie R. (1980) Shape effects on crystallite size distributions in synthetic hematites from X-ray line-profile analysis. *J. Solid State Chem.* **34**, 323–333.

Elsner M., Schwarzenbach R. P. and Haderlein S. (2004) Reactivity of Fe(II)-bearing minerals toward reductive transformation of organic contaminants. *Environ. Sci. Technol.* **38**, 799–807.

Frankel R. B., Papaefthymiou G. C., Blakemore R. P. and O'Brien W. (1983) Fe_3O_4 precipitation in magnetotactic bacteria. *Biochim. Biophys. Acta: Mol. Cell Res.* **763**, 147–159.

Garcell L., Morales M. P., Andres-Verges M., Tartaj P. and Serna C. J. (1998) Interfacial and rheological characteristics of maghemite aqueous suspensions. *J. Colloid Interface Sci.* **205**, 470–475.

Gorski C. A. and Scherer M. M. (2009) Influence of magnetite stoichiometry on Fe^{II} uptake and nitrobenzene reduction. *Environ. Sci. Technol.* **43**, 3675–3680.

Gregory K. B., Larese-Casanova P., Parkin G. F. and Scherer M. M. (2004) Abiotic transformation of hexahydro-1,3,5-trinitro-1,3,5-triazine by Fe^{II} bound to magnetite. *Environ. Sci. Technol.* **38**, 1408–1414.

Handler R. M., Beard B. L., Johnson C. M. and Scherer M. M. (2009) Atom exchange between aqueous Fe(II) and goethite: an Fe isotope tracer study. *Environ. Sci. Technol.* **43**, 1102–1107.

Hansel C. M., Benner S. G., Nico P. and Fendorf S. (2004) Structural constraints of ferric (hydr)oxides on dissimilatory iron reduction and the fate of Fe(II). *Geochim. Cosmochim. Acta* **68**, 3217–3229.

Hansel C. M., Benner S. G. and Fendorf S. (2005) Competing Fe(II)-induced mineralization pathways of ferrihydrite. *Environ. Sci. Technol.* **39**, 7147–7153.

Hartenbach A., Hofstetter T. B., Berg M., Bolotin J. and Schwarzenbach R. P. (2006) Using nitrogen isotope fractionation to assess abiotic reduction of nitroaromatic compounds. *Environ. Sci. Technol.* **40**, 7710–7716.

Hiemstra T. and van Riemsdijk W. H. (2007) Adsorption and surface oxidation of Fe(II) on metal (hydr)oxides. *Geochim. Cosmochim. Acta* **71**, 5913–5933.

Horio I., Zhou X. and Morrish A. H. (1994) Surface magnetic structure of $^{57}Fe^{2+}$ coated g-$^{56}Fe_2O_3$ particles with and without adsorbed cobalt. *J. Phys. Soc. Jpn.* **63**, 769–774.

Jeon B. H., Dempsey B. A., Burgos W. D., Royer R. A. and Roden E. E. (2004) Modeling the sorption kinetics of divalent metal ions to hematite. *Water Res.* **38**, 2499–2504.

Kerisit S. and Rosso K. M. (2006) Computer simulation of electron transfer at hematite surfaces. *Geochim. Cosmochim. Acta* **70**, 1888–1903.

Klausen J., Trober S. P., Haderlein S. B. and Schwarzenbach R. P. (1995) Reduction of substituted nitrobenzenes by Fe(II) in aqueous mineral suspensions. *Environ. Sci. Technol.* **29**, 2396–2404.

Klupinski T. P., Chin Y. and Traina S. J. (2004) Abiotic degradation of pentachlorobenzene by Fe(II): reactions on goethite and iron oxide nanoparticles. *Environ. Sci. Technol.* **38**, 4353–4360.

Konhauser K. O., Kappler A. and Roden E. E. (2011) Iron in microbial metabolisms. *Elements* **7**, 89–93.

Larese-Casanova P. and Scherer M. M. (2007a) Fe(II) sorption on hematite: new insights based on spectroscopic measurements. *Environ. Sci. Technol.* **41**, 471–477.

Larese-Casanova P. and Scherer M. M. (2007b) Morin transition suppression in polycrystalline ^{57}hematite (a-Fe_2O_3) exposed to $^{56}Fe(II)$. *Hyperfine Interact.* **174**, 111–119.

Larese-Casanova P., Cwiertny D. M. and Scherer M. M. (2010a) Nanogoethite formation from oxidation of Fe(II) sorbed on aluminum oxide: implications for contaminant reduction. *Environ. Sci. Technol.* **44**, 3765–3771.

Larese-Casanova P., Haderlein S. and Kappler A. (2010b) Lepidocrocite and goethite formation by nitrate-reducing Fe(II)-oxidizing bacteria: effect of pH, bicarbonate, phosphate and humic acids. *Geochim. Cosmochim. Acta* **74**, 3721–3734.

Lovley D. R. (1997) Microbial Fe(III) reduction in subsurface environments. *FEMS Microbiol. Rev.* **20**, 305–313.

Mikutta C., Wiederhold J. G., Cirpka O. A., Hofstetter T. B., Bourbon B. and Von Gunten U. (2009) Iron isotope fractionation and atom exchange during sorption of ferrous iron to mineral surfaces. *Geochim. Cosmochim. Acta* **73**, 1795–1812.

Morrish A. H. (1994) *Canted Antiferromagnetism: Hematite*. World Scientific, Singapore.

Murad E. and Cashion J. (2004) *Mossbauer Spectroscopy of Environmental Materials and Their Industrial Utilization*. Kluwer Academic Publishers.

Nano G. V. and Strathmann T. J. (2008) Application of surface complexation modeling to the reactivity of iron(II) with nitroaromatic and oxime carbamate contaminants. *J. Colloid Interface Sci.* **321**, 350–359.

Naono H., Nakai K., Sueyoshi T. and Yagi H. (1987) Porous texture in hematite derived from goethite: mechanism of thermal decomposition of geothite. *J. Colloid Interface Sci.* **120**, 439–450.

Nefso E. K., Burns S. E. and McGrath C. J. (2005) Degradation kinetics of TNT in the presence of six mineral surfaces and ferrous iron. *J. Hazard. Mater.* **123**, 79–88.

Park B. and Dempsey B. A. (2005) Heterogeneous oxidation of Fe(II) on ferric oxide at neutral pH and a low partial pressure of O_2. *Environ. Sci. Technol.* **39**, 6494–6500.

Pecher K., Haderlein S. B. and Schwarzenbach R. P. (2002) Reduction of polyhalogenated methanes by surface-bound Fe(II) in aqueous suspensions of iron oxides. *Environ. Sci. Technol.* **36**, 1734–1741.

Pedersen H. D., Postma D., Jakobsen R. and Larsen O. (2005) Fast transformation of iron oxyhydroxides by the catalytic action of aqueous Fe(II). *Geochim. Cosmochim. Acta* **69**, 3967–3977.

Peretyazhko T., Zachara J. M., Heald S. M., Kukkadapu R. K., Liu C., Plymale A. E. and Resch C. T. (2008) Reduction of Tc(VII) by Fe(II) sorbed on Al (hydr)oxides. *Environ. Sci. Technol.* **42**, 5499–5506.

Pivovarov S. (1997) Surface structure and site density of the oxide-solution interface. *J. Colloid Interface Sci.* **196**, 321–323.

Raming T. P., Winnubst A. J. A., van Kats C. M. and Philipse A. P. (2002) The synthesis and magnetic properties of nanosized hematite (α-Fe_2O_3) particles. *J. Colloid Interface Sci.* **249**, 346–350.

Rosso K. M., Smith D. M. A. and Dupuis M. (2003) An ab initio model of electron transport in hematite (a-Fe_2O_3) basal planes. *J. Chem. Phys.* **118**, 6455–6466.

Rosso K. M., Yanina S. V., Gorski C. A., Larese-Casanova P. and Scherer M. M. (2010) Connecting observations of hematite (a-Fe_2O_3) growth catalyzed by Fe(II). *Environ. Sci. Technol.* **44**, 61–67.

Rügge K., Hofstetter T. B., Haderlein S. B., Bjerg P. L., Knudsen S., Zraunig C., Mosbæk H. and Christensen T. H. (1998) Characterization of predominant reductants in an anaerobic leachate-contaminated aquifer by nitroaromatic probe compounds. *Environ. Sci. Technol.* **32**, 23–31.

Schaefer M. V., Gorski C. A. and Scherer M. M. (2011) Spectroscopic evidence for interfacial Fe(II)–Fe(III) electron transfer in a clay mineral. *Environ. Sci. Technol.* **45**, 540–545.

Scherer M. M., Balko B. A. and Tratnyek P. G. (1999) The role of oxides in reduction reactions at the metal–water interface. In *Mineral–Water Interfacial Reactions*. American Chemical Society, pp. 301–322.

Schultz C. A. and Grundl T. (2000) PH dependence on reduction rate of 4-Cl-nitrobenzene by Fe(II)/montmorillonite systems. *Environ. Sci. Technol.* **34**, 3641–3648.

Schwertmann U. and Cornell R. M. (2000) *Iron Oxides in the Laboratory: Preparation and Characterization*. Wiley-VCH Verlag GmbH, Weinheim.

Sherman D. M. (1987) Molecular orbital (SCF-Xa-SW) theory of metal–metal charge transfer process in minerals. *Phys. Chem. Miner.* **14**, 355–363.

Silvester E., Charlet L., Tournassat C., Géhin A., Grenèche J. and Liger E. (2005) Redox potential measurements and Mössbauer spectrometry of Fe^{II} adsorbed onto Fe^{III} (oxyhydr)oxides. *Geochim. Cosmochim. Acta* **69**, 4801–4815.

Sorensen J. and Thorling L. (1991) Stimulation by lepidocrocite (y-FeOOH) of Fe(II)-dependent nitrite reduction. *Geochim. Cosmochim. Acta* **55**, 1289–1294.

Stookey L. L. (1970) Ferrozine—a new spectrophotometric reagent for iron. *Anal. Chem.* **42**, 779–781.

Strathmann T. J. and Stone A. T. (2003) Mineral surface catalysis of reactions between Fe^{II} and oxime carbamate pesticides. *Geochim. Cosmochim. Acta* **67**, 2775–2791.

Sugimoto T. and Wang Y. (1998) Mechanism of the shape and structure control of monodispersed α-Fe_2O_3 particles by sulfate ions. *J. Colloid Interface Sci.* **207**, 137–149.

Tamura H., Matijevic E. and Meites L. (1983) Adsorption of Co^{2+} ions on spherical magnetite particles. *J. Colloid Interface Sci.* **92**, 303–314.

Thompson A., Chadwick O. A., Rancourt D. G. and Chorover J. (2006) Iron-oxide crystallinity increases during soil redox oscillations. *Geochim. Cosmochim. Acta* **70**, 1710–1727.

Thompson A., Rancourt D. G., Chadwick O. A. and Chorover J. (2011) Iron solid-phase differentiation along a redox gradient in basaltic soils. *Geochim. Cosmochim. Acta* **75**, 119–133.

Tronc E., Jolivet J. P., Lefebvre J., Tabatabai M. A. and Massart R. (1984). *J. Chem. Soc., Faraday Trans. 1* **80**, 2619.

Vandenberghe R. E., Barrero C. A., da Costa G. M., Van San E. and De Grave E. (2000) Mossbauer characterization of iron oxides and (oxy)hydroxides: the present state of the art. *Hyperfine Interact.* **126**, 247–259.

Williams A. G. B. and Scherer M. M. (2004) Spectroscopic evidence for Fe(II)–Fe(III) electron transfer at the Fe oxide–water interface. *Environ. Sci. Technol.* **38**, 4782–4790.

Yanina S. V. and Rosso K. (2008) Linked reactivity at mineral–water interfaces through bulk crystal conduction. *Science* **320**, 218–222.

Zhang Y., Charlet L. and Schindler P. W. (1992) Adsorption of protons, Fe(II) and Al(III) on lepidocrocite (γ-FeOOH). *Colloids Surf.* **63**, 259–268.

Zwank L., Elsner M., Aeberhard A., Schwarzenbach R. P. and Haderlein S. B. (2005) Carbon isotope fractionation in the reductive dehalogenation of carbon tetrachloride at iron (hydr)oxide and iron sulfide minerals. *Environ. Sci. Technol.* **39**, 5634–5641.

Associate editor: Christopher John Daughney